RSC Advances

PAPER

View Article Online
View Journal | View Issue

Cite this: *RSC Adv.*, 2024, **14**, 13053

Effects of external light in the magnetic field-modulated photocatalytic reactions in a microfluidic chip reactor

Hung Ji Huang, *[a] Yen Han Wang,[b] Xuan-Yu Shih,[a] Sy-Hann Chen,[c] Hai-Pang Chiang,[d] Yuan-Fong Chou Chau[e] and Jeffrey Chi-Sheng Wu [b]

Received 16th January 2024
Accepted 15th April 2024

DOI: 10.1039/d4ra00415a

rsc.li/rsc-advances

Photocatalytic reactions and their magnetic-field enhancement present significant potential for practical applications in green chemistry. This work presents the mutual enhancement of plasmonic photocatalytic reaction by externally applied magnetic field and plasmonic enhancement in a micro optofluidic chip reactor. The tiny gold (Au) nanoparticles of only a few atoms fixed on the surface of titanium dioxide (TiO_2) nanoparticles lead to mutually boosted enhancement photocatalytic reactions under an external magnetic field and plasmonic effects. The dominant factor of adding green light to the photocatalytic reaction leads to the understanding that it is a plasmonic effect. The positive results of adding ethanol alcohol (EA) in the experiments further present that it is a hot electron dominant path photocatalytic reaction that is positively enhanced by both the external magnetic field and plasmonic effects. This work offers great potential for utilizing magnetic field enhancement in plasmonic photocatalytic reactions.

Introduction

Surface plasmons[1–3] are the wave modes of light at the interface between negative (metal) and positive (dielectric or semiconductor) permittivity materials. The induced plasmon energy on a metal nanoparticle can be delivered elastically or inelastically by transferring light energy to nearby materials.[3] Optical scattering and trapping by metal nanoparticles to the nearby photocatalysts can increase the photon flux flow through photocatalytic nanoparticles,[4–10] thus enhancing the photocatalytic reaction through the plasmon elastic decay path. On the other hand, numerous inelastic decay paths, *e.g.*, plasmon-induced energy transformation (PIRET),[6,11,12] quantum hot-charge carriers (QHCs),[6,13–18] or simply plasmonic-heating, also enhance photocatalytic reactions. The indirect or direct heating by induced plasmons can increase the local temperature to enhance the photocatalytic reactions, which the Arrhenius equation can explain.[16]

By a unique inelastic decay path, the generated plasmon can be transformed into quantum hot-charge carriers (QHCs) through Landau damping with intraband and interband electron transitions under the quantum confinement of a few nanometer-sized metal particles.[6,13–19] Plasmonic hot-carrier collection over a tunable Schottky barrier enables additional energy harvesting at a metal–semiconductor interface, while gold produces holes hotter than electrons by 1–2 eV.[20] The additional harvested energy can compensate for the energy in the photocatalytic reactions.[9] The decorated metal nanoparticles lead to highly efficient plasmonic photocatalytic reactions through enhanced light energy harvesting and conversion efficiency.

Various paths of energy transformation or mechanisms, including chemical and physical models, are used to explain the enhancement of plasmonic photocatalysis.[6] Different experimental setups can selectively identify the mechanism of plasmonic enhancement in photocatalytic reactions.[16] However, the plasmonic effects on photocatalysis are still an intriguing field that can interfere with other physical phenomena and is not easy to understand.

The enhancement by an externally applied magnetic field of photocatalytic reactions[17,21–26] is also a difficult-to-understand research topic.[27–30] At the beginning of relative research works, some composite photocatalysts containing magnetic nanomaterials have attracted considerable interest as they can be easily collected and recycled after use. Wakasa's group later discovered that the non-magnetic photocatalyst TiO_2 presents improved processing efficiency under an external magnetic

[a]*Department of Electro-Optical Engineering, National Formosa University, Yunlin 632, Taiwan. E-mail: hjhuang@nfu.edu.tw*

[b]*Department of Chemical Engineering, National Taiwan University, Taipei 10617, Taiwan*

[c]*Department of Electrophysics, National Chiayi University, Chiayi 600, Taiwan*

[d]*Department of Optoelectronics and Materials Technology, National Taiwan Ocean University, Keelung 20224, Taiwan*

[e]*Centre for Advanced Material and Energy Sciences, Universiti Brunei Darussalam, Brunei Darussalam*

field.[23] This important and environmentally beneficial method is easy to continuously process by adding an external magnetic field by magnets to enhance the photocatalytic reactions without extra power consumption.[21,22]

After this, many novel works have applied additional magnetic fields to enhance photocatalytic reactions. A ferromagnetic $ZnFe_2O_4$ (ZFO) photoelectrode with improved ferromagnetic property performance significant enhancement of high-efficiency photoelectrochemical process that assigned to electron spin polarization of the ferromagnetic ZFO photoelectrode regulated by the magnetic field.[31] The spin state loss of excited electrons leads to numerous photoinduced electrons in the same spin state as holes and unfavorable recombination during light excitation. The chiral structure in zinc oxide (ZnO) can induce the spin selectivity effect to promote photocatalytic performance.[32] The polarized carriers possess a prolonged carrier lifetime and increase the triplet species instead of singlet byproducts during the reactions, *i.e.*, higher activity contaminant photodegradation than the achiral ZnO. The magnetic field-derived spin polarization reduced the charge recombination in cadmium sulfide (CdS).[33] It improved the interface transfer efficiency between CdS and molybdenum disulfide (MoS_2), which resulted in a 3.89-fold improvement of the photocatalytic hydrogen production under an external magnetic field. The magnetic field-regulated spin polarization further explains the coupling between the magnetic field and photocatalytic activity.[34] The transition of the electron-spin state contributes to charge transfer within the photocatalyst.[35] At the same time, spin polarization can promote the orbital interaction between the catalyst and reactants/intermediates for binding to the reactants, promoting the formation of reactive oxygen species.[36]

A magnetic field can also conduct the Lorentz force, which effectively regulates the separation and transfer of photogenerated carriers in the photocatalytic process.[37,38] Thus, the lifetime of the hot charge carriers is prolonged to trigger more photocatalytic reactions.

The plasmonic effect and the magnetic field enhancement are separately demonstrated to enhance photocatalytic reactions. However, are they able to combine to enhance the photocatalytic reactions? The applied magnetic field can modulate the generated hot charge carriers or surface plasmon polaritons. However, the magnetic alignment of the intrinsic spin of the holes or electrons can also be disturbed by plasmonic heating on metal nanoparticles. What if and how were the external magnetic field and the plasmonic effects involved in the same experimental setup?

In this paper, we present an experimental setup for studying the corporate effects of magnetic field and plasmonic enhancement in a micro optofluidic chip reactor (MOFC)[21,39] that is beneficial in small size, low power consumption and little waste in the modern framework of green chemistry. The transparent glass substrate of the chip reactor allows ultraviolet (UV) light to enter from beneath and can also be used as a planner waveguide to supply optical energy of visible light. Using waveguides to deliver energy can increase the harvest efficiency of visible light for photocatalytic reactions.[8] The propagating visible light illuminates the deposited Au–TiO_2 through numerous internal reflections inside the plane waveguide.

Furthermore, in longtime experiments the small chip size of several centimeters allows an easy setup of magnet pairs for a stable magnetic field in a defined direction.[16,21] Based on experimental results, we present the mutual enhancement of the plasmonic effect and apply an external magnetic field to the photocatalytic reactions on Au–TiO_2 nanoparticles.

Results and discussion

Material analysis

On the chip substrate of the MOFC reactor, the pre-deposited P25 TiO_2 nanoparticles (Degussa, Sigma-Aldrich) were decorated with Au (gold) nanoparticles by UV light-assisted reduction of Au^+ ions. The decorated Au nanoparticles mediated the light energy harvest and conversion in some processes with the illumination of UV light and selectively provided visible light of various colors.

Fig. 1(a) presents the surface morphology and microstructure of photocatalysts by transmission electron microscope (TEM). The granular particle size of the Au–TiO_2 nanoparticles was primarily around 23 nm, resembling that from the commercial data. The TEM image cannot identify the decorated Au nanoparticles (NPs). The energy-dispersive X-ray spectroscopy (EDS) measurement in Fig. 1(b) presents that the Au existed but was lower than 0.5 weight percentage (wt%). This means the Au NPs were unobservable tiny nanoparticles or just fixed atoms on the surface of TiO_2 NPs. Therefore, it is challenging to find Au NPs even in TEM measurements.

As shown in Fig. 1(c), the X-ray diffraction (XRD) measurements can only observe the original diffraction peaks of anatase and rutile of commercial P25 TiO_2 that are denoted as "a" and

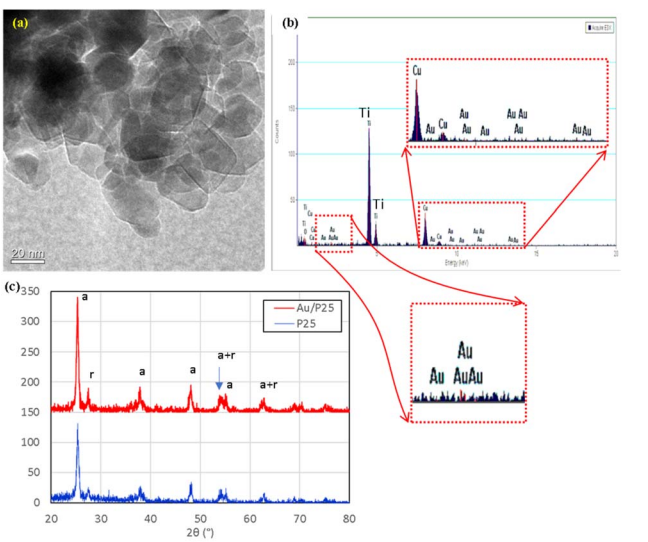

Fig. 1 (a) Transmission image, (b) EDS in TEM measurements, and (c) XRD measurements of Au–TiO_2 nanoparticles. The embedded pictures provide details of Au's tiny peaks.

"r," respectively. The major anatase peaks (JCPDS 21-1272) can be found at 25.281°, 36.946°, 37.8°, 38.575°, 48.049°, 53.89°, 55.06°, 62.688°, 68.76°, and 75.029°. The major rutile peaks (JCPDS 21-1276) can be found at 27.446°, 36.085°, 54.322°, 64.038°, and 69.008°. No apparent Au peaks were found in the XRD measurements due to a loading lower than 0.5 wt%, high dispersion, or low crystallinity. Therefore, the photo-synthesized decoration process of Au NPs makes little difference in the crystal structure of the TiO_2 NPs. Only the peaks of TiO_2 were observed.

X-ray photoelectron spectroscopy (XPS) was performed further to identify the chemical states of Au–TiO_2 NPs with various binding energies (B.E.), as shown in Fig. 2. The survey spectrum in Fig. 2(a) revealed the presence of Au 4f, Ti 2p, O 1s, and C 1s. The other peaks are ascribed to different orbitals and auger electrons from the above elements. The C 1s peak was from the adventitious impurities. Fig. 5(b) shows that the dominant peaks at binding energy 458.7 and 464.5 eV were Ti^{4+} $2p_{3/2}$ and $2p_{1/2}$ from titanium dioxide,[40] with a splitting width of around 5.5 eV.[41]

In Fig. 2(c), the peaks at binding energy 83.1 and 86.8 eV indicated the doublet of metallic Au, while the peaks at 83.5 and 88.5 eV were attributed to the doublet of Au^{+}. The peaks of Au^{3+} were not identified in the result of the fitting date. The results show that the Au^{3+} ions were reduced to Au^{0} or Au^{+} and fixed on the surface of the TiO_2 nanoparticles. The unreduced Au^{3+} ions were flushed away by deionized (DI) water cleaning in the sample preparation processes. The covered volume of the Au peaks was much lower than that of Ti peaks and presented a very low loaded wt% of Au. The results resemble that of EDS measurements and XRD measurements. Only very tiny Au particles or atoms are fixed on the surface of TiO_2 NPs.

Spectral measurements

UV-visible diffuse reflectance spectroscopy is used to measure the optical absorbance of the photocatalysts, as shown in Fig. 3(a). TiO_2 absorbed light from 300 nm to 400 nm, while additional loading of Au NPs led to the slight enhancement of visible light harvesting from 400 to 800 nm. As shown in Fig. 3(b), the difference in absorbance between Au–TiO_2 and TiO_2 samples in Fig. 3(a) is very small. However, the typical plasmonic absorption peak at around 550 nm is identifiable in Fig. 3(b), depicting the presence of decorated metal gold nanoparticles. Due to the meager loading quantity of Au nanoparticles, the enhancement of light absorbance is minimal in the visible light region. However, the absorbance enhancement of 300–350 nm UV light is much more significant than the visible light band. This also shows that the decorated Au nanoparticles are much more likely to be diverse tiny islands of few atoms on the surface of TiO_2 nanoparticles. Decorated Au nanoparticles of the Au–TiO_2 sample increase the light harvest efficiency of wavelength from 300 nm to 350 nm compared to that of pure TiO_2. This is the plasmonic trapping/focusing effect of Au nanoparticles. As shown in Fig. 3(c), the Tauc plot with linear fitting converted from the absorbance spectrum indicates that the bandgap of the TiO_2 or Au–TiO_2 nanoparticles is all around 3.1 eV. Due to the limitation of the direct deposition method, the deposited TiO_2 layers are thin and can be stably fixed on glass. The absorbance spectrum is the mixed effects of a thin TiO_2 porous layer and the glass substrate, with the fitting value slightly smaller than typical P25 TiO_2 nanoparticles.[42] However, the thin deposition thickness of the TiO_2 layer can lead to an averaged chance of getting the diffused Au^{3+} ions from the $HAuCl_4$ solution in the Au nanoparticles decoration process.

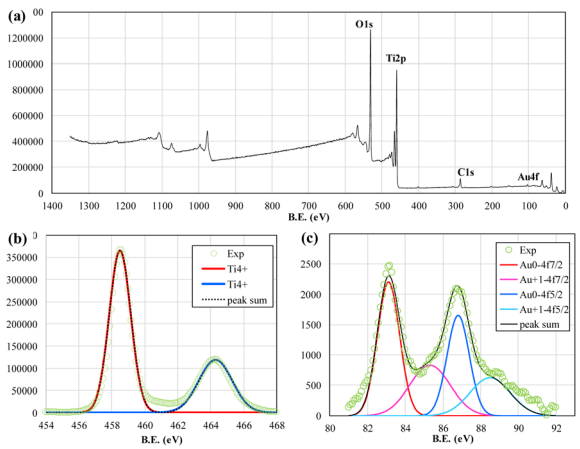

Fig. 2 (a) Survey scan, (b) Ti peaks, and (c) Au peaks in XPS data.

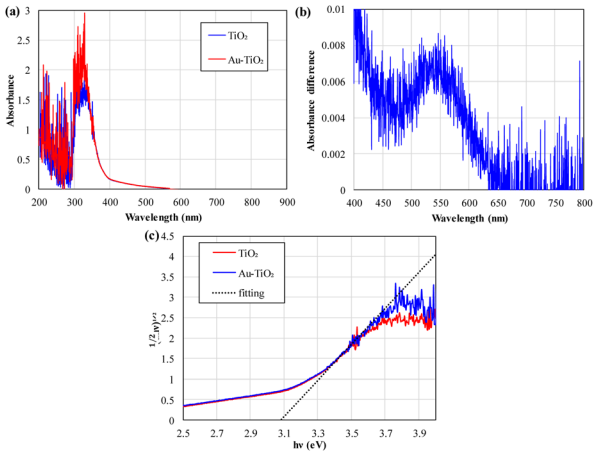

Fig. 3 (a) Absorbance spectrum, (b) difference in absorbance by "Au–TiO_2," and (c) Tauc plot of TiO_2 and Au–TiO_2 nanoparticles.

Magnetic hysteresis measurements

The magnetization of the TiO_2 and Au–TiO_2 in various magnetic fields circulating two runs presents anti-ferromagnetic responses in magnetic hysteresis (Fig. 4). No apparent magnetization hysteresis effect exists under a 12 000 Oe external magnetic field.

Photocatalytic reaction

The experimental results, see Fig. 5(a), presented the effective photocatalytic degradation of methyl orange (MO, $C_o = 10$ μM

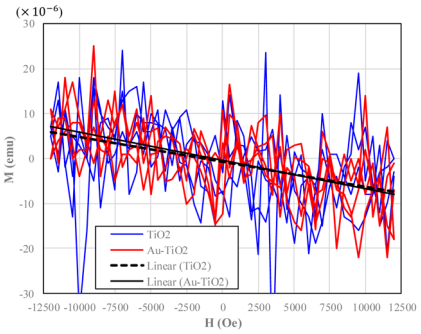

Fig. 4 Hysteresis curve of TiO_2 and Au–TiO_2. The effects of the glass substrate have been removed.

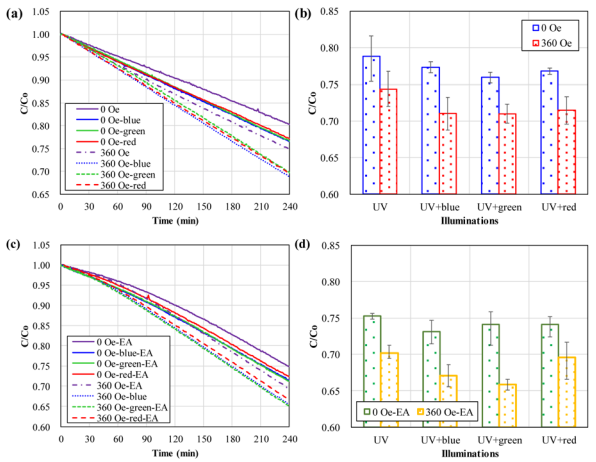

Fig. 5 (a) Four hours of photocatalytic degradation of MO under various light illumination and with or without an external magnetic field. (b) Statistical data on photocatalytic MO degradation under different light illuminations and with or without an external magnetic field. (c) Four hours of photocatalytic degradation of MO "with EA" under various light illumination and with or without an external magnetic field. (d) Statistical data on photocatalytic MO degradation "with EA" under different light illumination and with or without an external magnetic field.

in origin) dissolved in water processed by 254 nm UV light illumination on Au–TiO_2 nanoparticles. The experiments are processed with a sequential circulation of the various arrangements. The average and errors of experimental results for various arrangements present a consistent performance of the magnetic field-modulated plasmonic photocatalytic reactions.

With 4 hours of processes, the reserved MO concentration ratio (C/C_o) decreased to about 0.7–0.8. "UV" denotes that all the experiments were processed with 254 nm UV light illumination. The experiments processed "without" and "with" 360 Oe external magnetic fields and are marked as solid and dashed lines, respectively. Blue, green, and red colors mark the experiments with the illuminations of additional visible light from various color light emitting diodes (LEDs).

As shown in Fig. 5(b), the data from numerous experimental runs presents the plasmonic enhancement of the photocatalytic degradation of MO molecules in solution under additional illumination of red, green, and blue visible light. The additionally applied magnetic field can further strengthen the plasmonic enhancement of photocatalytic reactions.

In the experiments of additional dissolved EA, as shown in Fig. 5(c) and (d), the MO concentrations of various experiments were also decreased with the increased processing time. With 4 hours of processes, the MO concentration ratio (C/C_o) decreased to about 0.65–0.75. "EA" denotes the experiments processed by adding EA to the solution. In the experiments with EA but without an external magnetic field, as shown in Fig. 5(b), the additional illumination of visible light, on average, presents little effect on the photocatalytic reactions. The extra blue light illumination had a slightly better enhancement, but only 1%.

However, in the experiments of external magnetic field and additional EA, the additional blue and green light led to a 3–4% further enhancement of the plasmonic photocatalytic degradation of MO. The numerous experimental data, on average, presented that the external magnetic field, the dissolved EA, and the additional visible-light-induced plasmonic effects positively enhanced the photocatalytic degradation of MO in combination.

The light scattering/trapping effect of decorated Au nanoparticles (0.5 nm in diameter), as shown in Fig. 6(a)–(h), substantially enhanced field intensity around and in the TiO_2 nanoparticles (22 nm in diameter).

In a specific polarization, E_z, the 254 nm background light of 1 V m^{-1} in origin propagation in the positive z-direction can be enlarged to 2 V m^{-1} even by a 0.5 nm tiny Au nanoparticle at the adjacent area; see Fig. 6(b). Furthermore, the 518 nm light can be trapped on the decorated Au nanoparticles and introduce plasmonic energy transformation for plasmonic photocatalytic reactions. The calculated loss spectra of Au and TiO_2 nanoparticles, as shown in Fig. 6(i), present their selective utilization of visible and UV light, respectively. In our experience, the larger or more TiO_2 nanoparticles will have a similar energy loss spectrum resembling the absorbance spectrum in Fig. 3(a).

The photocatalytic degradation of MO proceeds in the following steps:

$$TiO_2 + h\nu \rightarrow TiO_2\,(hVB^+) + TiO_2\,(eCB^-)$$

$$TiO_2\,(hVB^+) + H_2O \rightarrow TiO_2 + H^+ + OH^-$$

$$TiO_2\,(hVB^+) + OH^- \rightarrow TiO_2 + {}^*OH$$

$$\text{Dye} + {}^*OH \rightarrow \text{degradation products}$$

$$TiO_2\,(eCB^-) + O_2 \rightarrow TiO_2 + {}^*O^{2-}$$

$${}^*O^{2-} + H^+ \rightarrow {}^*HO^{2-}$$

$$\text{Dye} + {}^*HO^{2-} \rightarrow \text{degradation products.}$$

Adding EA to the solution positively enhances the plasmonic photocatalytic reactions in this work. EA is typically the hot hole scavenger in photocatalytic reactions by TiO_2 nanoparticles. The prohibition of the hot hole reaction path usually leads to

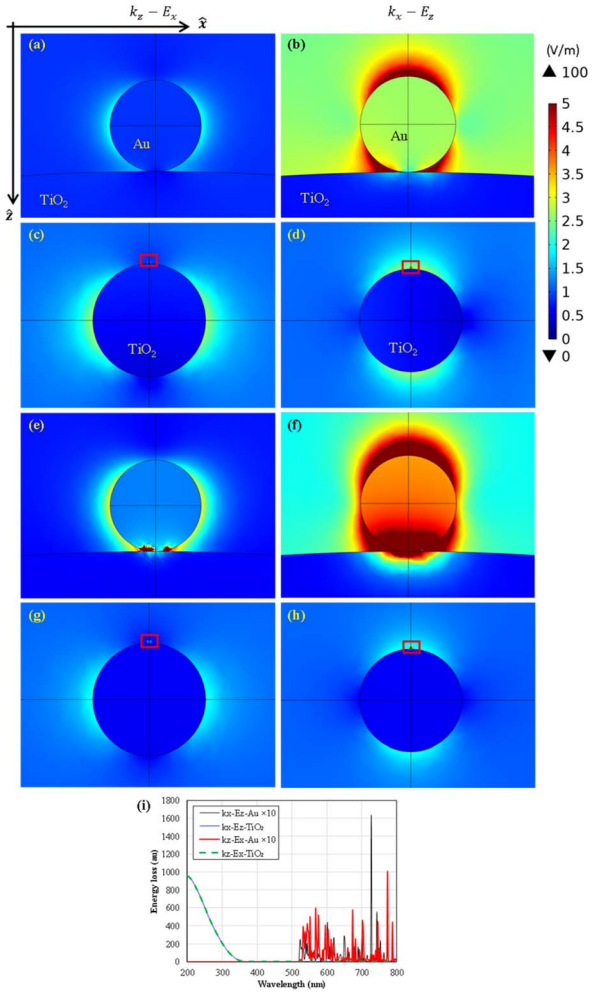

Fig. 6 Finite element numerical calculation of scattering electric field intensity of 254 nm incident light that incident at *z* (a), (c) and *x* (b), (d) direction, and 512 nm incident light that incident at *z* (e), (g) and *x* (f), (h) direction. (a), (b), (e) and (f) are the zoom-in pictures of the red rectangular area marked in (c), (d), (g) and (h), respectively. (i) Calculated energy loss spectra of the Au and TiO_2 nanoparticles.

a decreased photocatalytic processing efficiency. This can be seen in the previous works by pure TiO_2 nanoparticles in the same system.[21]

However, adding EA positively enhances the plasmonic photocatalytic reactions processed with Au-decorated TiO_2 nanoparticles. The fixed tiny Au nanoparticles alter the photocatalytic reaction path from the hot hole path dominant process for pure TiO_2 nanoparticles to the hot electron path dominant process for Au–TiO_2 nanoparticles. As shown in Fig. 3, the absorbance spectrum of tiny Au nanoparticles presents the potential to generate more and trap the UV light-induced hot electrons and enhance the photocatalytic degradation of methyl orange in solution. The spectral measurements in Fig. 3 present the extra absorption of UV light at 300–350 nm, thus also leading to an enhanced photocatalytic reaction by Au–TiO_2 nanoparticles. The addition of EA further reduces the generated hot holes in the TiO_2 side and reduces the recombination and attraction with the hot electrons.

Furthermore, the photocatalytic processing efficiency reached a maximum average value with the additional green LED illumination among all the experiments in this work. The application of red and blue light did not present a meaningful enhancement. Greenlight is the typical plasma frequency of Au. This means that even though the size of the decorated Au nanoparticles is too small to be identified in material characterization results, they also have a low but meaningful optical response. This can also be observed in spectral measurements in Fig. 3 and numerical calculations in Fig. 6(i).

The photocatalyst used in this work is mostly TiO_2. Therefore, UV light is crucial in triggering the photocatalytic reaction. However, this work demonstrates that additional visible light illuminations can further boost the photocatalytic reaction, even with decorated gold nanoparticles lower than 0.5 wt%. This means that the photocatalyst of Au–TiO_2 composites will be more efficient than pure TiO_2 under sunlight illuminations of visible light. The 0.5 wt% decoration of gold will only add a little cost to the fabrication processes of the photocatalyst but introduces a potential possibility to enhance photocatalytic reactions.

The boosting mechanism of the photocatalytic reaction is crucial in this work. We are going to discuss it in several viewpoints.

Typically, the decorated Au metal nanoparticles with low potential energy can be a reservoir of the induced hot electrons generated on the contacted TiO_2 nanoparticles under 254 nm UV light illumination. The generated plasmons on decorated Au nanoparticles can enhance plasmonic photocatalysis in various energy transformation paths.[16] The additional light energy may not be able to induce the photocatalytic reaction directly but can compensate for the required chemical energy.[9] As shown in Fig. 7, in Au–TiO_2 systems of the TiO_2 nanoparticles with the decorated few-atoms Au nanoparticles, the hot electron path is the dominant process that can be strengthened by applying plasmonic electromagnetic energy. The added EA can attract and reduce the UV light-generated hot holes. The hot electrons are more likely to be reserved for the reaction's dominant path on "Au–TiO_2 nanoparticles". The additional green visible light can compensate for the insufficient chemical energy and enhance the plasmonic photocatalytic reactions through a hot electron path on decorated Au nanoparticles.

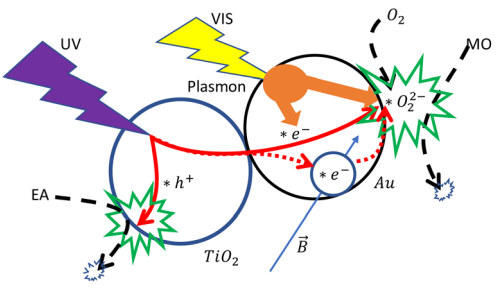

Fig. 7 Schematics presents the proposed mechanism of the magnetic field-affected plasmonic photocatalytic reaction.

The experimental data also presents observable magnetic field enhancement of plasmonic photocatalytic reactions, *i.e.*, the experiments of both additional visible light and external magnetic field offer the best photocatalysis efficiency. The experimental results show that the externally applied magnetic field can strengthen the dominant plasmonic enhancement paths in photocatalytic reactions in the Au–TiO_2 hybrid nanoparticles in this work. From a typical viewpoint, applying additional visible light can create localized surface plasmons on the decorated Au nanoparticles through plasmonic heating.[16,43] The increased local temperature can limit the magnetic field effect. However, this did not happen in the photocatalytic reactions in this work.

By a special inelastic decay path, the generated plasmon can be transformed into quantum hot-charge carriers (QHCs) through Landau damping with intraband and interband electron transitions under the quantum confinement of a few nanometer-sized metal particles.[6,13–19] The effects of the singlet-triplet intersystem crossing of radicals and the Lorentz force further suppressing the recombination of photogenerated electrons and holes can enhance the photocatalytic reactions when introducing an external magnetic field.[22] Plasmonic hot-carrier collection over a tunable Schottky barrier enables additional energy harvesting at a metal–semiconductor interface, while gold produces holes hotter than electrons by 1–2 eV.[20] The additional harvested energy can compensate for the energy in the photocatalytic reactions.[9] The decorated metal nanoparticles lead to highly efficient plasmonic photocatalytic reactions through enhanced light energy harvesting and conversion efficiency.

By applying an external magnetic field, the spin polarization can also promote the orbital interaction between the catalyst and reactants/intermediates for binding to the reactants, promote the formation of reactive oxygen species,[36] and increase the triplet species instead of singlet byproducts[32] for higher activity contaminant photodegradation. The tiny-sized Au nanoparticles can be quantum wells for plasmon conversion to high-energy quantum hot charge carriers that compensate for the energy needed to break through the chemical potentials of the photocatalytic reactions.[16,20,44] Applying an external magnetic field can also introduce the induced spin selectivity that can enhance the photocatalytic reactions by prolonging the generated hot charge-carrier lifetime by reducing the charge recombination process.[31–33] The transition of the electron-spin state contributes to charge transfer within the photocatalyst conducting the Lorentz force.[35,37,38] It improves the interface transfer efficiency,[33] which allows more polarized charge traveling between TiO_2 and decorated Au nanoparticles. The quantum hot electrons aligned by the external magnetic field thus further enhance the photocatalytic reactions by the energy of visible light.

Therefore, light-generated hot electrons tend to move to decorated low-potential Au nanoparticles for advanced enhancement of photocatalytic reactions. The QHC generation under a magnetic field is believed to be converted to polarized charges of additional compensated energies. Applying an external magnetic field thus further enhances the plasmonic photocatalytic reactions. Introducing ethanol alcohol as the hole scavenger quickly reduces the light-generated holes and the recombination of high-activity hot electrons. Therefore, light-generated hot electrons are the dominant path and can be enhanced by additional visible-light-driven plasmonic and magnetic field-driven spin-polarization effects.

Experimental

Synthesis of material

A blank glass slide was used as the substrate of the MOFC reactor. The 0.1 g P25 TiO_2 NPs were homogenously dispensed in the 100 mL DI water and stirred to a homogeneously suspended gel solution. The P25 gel solution of suitable volume ($\sim$0.5 mL) was carefully dropped to the area (15×25 mm^2) on the glass slide of no tape protection and dried in ambient condition with a cover of a plastic Petri dish for several days. The protection tape was later removed when the TiO_2 layer was dehydrated.

The homogeneously deposited layer of P25 TiO_2 nanoparticles was then decorated with Au nanoparticles by UV light-assisted reduction of Au^+ ions. The samples of the TiO_2 layer were illuminated with 254 nm UV light from a 4 W mercury tube lamp for 20 min. When the 254 nm UV light was turned off, a suitable volume of $HAuCl_4$ solution was then dropped on the activated TiO_2 layer and kept static with a plastic Petri dish cover in ambient condition for another 20 min. The Au^+ ions can get the light-generated hot electrons on the TiO_2 NPs to fabricate tiny decorated Au NPs.[45] After that, the sample glass substrate with Au–TiO_2 deposited layer was cleaned with dilute ion water, dried at 60 °C, baked on a hot plate in the air, and ready to fabricate the MOFC reactor.

The Au decorated TiO_2 (Au–TiO_2) samples were characterized by the material analysis tools, transmission electron microscope (TEM, Hitachi S-4800), X-ray diffraction (XRD, Rigaku SmartLab SE), X-ray photoelectron spectroscopy (XPS, Thermo Scientific). The TEM inspection provides details of material structures and energy-dispersive X-ray spectroscopy (EDS) analysis to allocate the decorated Au NPs. The XRD analysis helps to characterize the crystal of the synthesized nanoparticles with Cu Kα irradiation in the range of 10° to 80°. The XPS measurement provides details of the surface elemental composition of photocatalysts on the theta probe. The optical responses of the fabricated samples were also characterized by a UV-visible light spectrometer (Agilent Carry 300).

Photocatalytic reaction

This work introduced a dual-light source MOFC reactor to process magnetic field-modulated plasmonic photocatalytic reactions, as shown in Fig. 8. Using a high-efficiency MOFC reactor aims to set up a thin micro-planar flow under light illumination and the application of the magnetic field. This makes it capable of revealing the effects of a magnetic field in a specific direction and the plasmonic effects.

The closed-loop MOFC[21] was constructed with a substrate of a typical glass slide and a plastic cape with sunken structures to

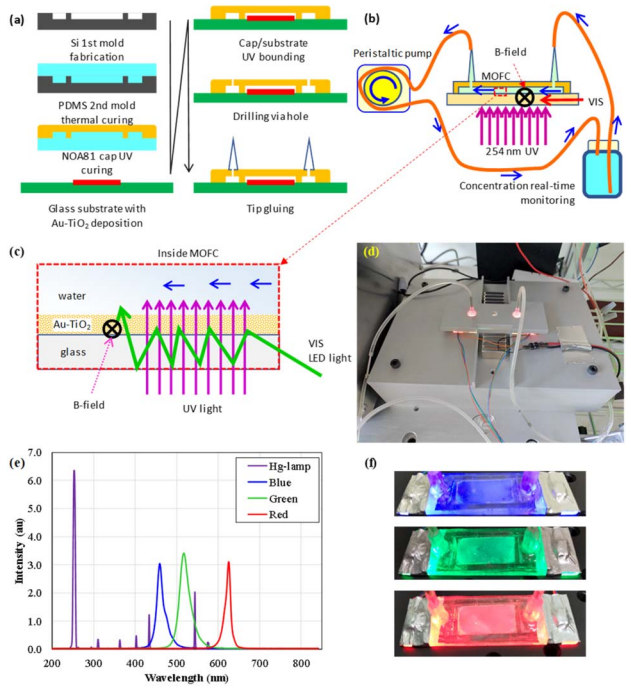

Fig. 8 Schematics of (a) chip fabrication process, (b) experimental setup of photocatalytic reaction, (c) light illumination and magnetic field arrangement inside the MOFC reactor. (d) Picture of the experimental facilities. (e) Intensity spectra of various light sources, including those from the Hg tube lamp and the blue, green, and red LEDs. (f) It is the same MOFC reactor that turns on different LEDs.

define the rectangular fluidic channel. The plastic cap was fabricated by UV-cured glue (the UV-curable Norland Optical Adhesive; NOA81) on a pre-structured polydimethylsiloxane (PDMS) mold. The system's design includes a MOFC, magnets for supplying a static magnetic field, a UV light source to provide energy for photocatalytic reactions, a micro-fluidic circulation pump, and a recording system to read out the real-time concentration of methyl orange.

Fig. 1(a) shows that a silicon-based first mold was produced *via* ICP deep dry-etching to fabricate the chip reactor after a SiO_2 hard mask was prepared. The mold was heated to 75 °C for 20 min to solidify the covered thick polydimethylsiloxane (PDMS) layer as the second mold.

The NOA81 polymer cap was fabricated using the PDMS mold under UV light illumination. The NOA81 polymer cap layer was quickly stripped from the PDMS mold, fixed on a glass slide of pre-deposited Au–TiO_2 layer for further UV light illumination, and solidified. Next, two holes were drilled into the NOA81-capped layer, where micro-tips were glued using NOA81 for the test solution to flow in and out of the micro reaction area.

On the chip substrate, the pre-deposited P25 TiO_2 nanoparticles were decorated with Au nanoparticles by UV light-assisted reduction of Au^+ ions before fixing the fabricated NOA81 cap. The decorated Au nanoparticles mediated the light energy harvest and conversion in some processes selectively illuminated with UV light and additional visible light of various colors.

Fig. 8(b) and (d) presents the schematics and a picture of the experimental setup. A 4 W low-pressure mercury tube lamp beneath the chip substrate provides 254 nm UV light to trigger the TiO_2 nanoparticles' photocatalytic reaction directly. The selective addition of visible lights from red, green, and blue LEDs, as shown in Fig. 8(c), (e) and (f), triggers plasmonic heating or energy compensation to enhance the photocatalytic reactions further. The glass substrate of the chip reactor can also be used as a planner waveguide to supply optical energy. The visible lights were guided inside the plane chip substrate to reduce the absorptions by the target pollutes of methyl orange dissolved in the test solution. In the various preliminary tests, the direct illumination of visible light can lead to quick decay of the low-pressure mercury lamp. Therefore, the UV and visible lights were arranged for delivery in two different paths. The experimental setup of the dual light sources presents plasmonic effects under UV light with or without various additional visible lights.

As shown in Fig. 8(b), the methyl orange (MO) test solution was circulated in a closed fluid system consisting of tubing (TYGON E-3603 tubing, Saint-Gobain Performance Plastics, USA) and a 25 mL glass bottle reservoir. A peristaltic pump propelled the four-hour flow circulation processes of the photocatalytic reaction per experiment by turning on various light sources. The transmission of 465 nm blue light through the glass reservoir measured the reserved concentration of the methyl orange molecules every minute.

For an advanced understanding of the effects of hot charge carriers by plasmonic enhancements and magnetic field effect on the photocatalytic reaction, additional experiments were conducted with another 0.16 mL extra absolute ethanol alcohol (EA) in the 20 mL test solution. EA is the scavenger of the UV light-generated hot holes (hVB^+) in TiO_2. In these experiments, adding ethanol alcohol eliminates chemical process steps (2)–(4). On the other hand, the recombination of the hot charge pairs is also eliminated due to the removal of the generated hot holes. More hot electrons (eCB^-) can be used in the photocatalytic reactions.

Fig. 8(b) shows four pairs of neodymium magnets supplying an external magnetic field of about 360 Oe parallel to the chip substrate surface and perpendicular to the fluid direction. An additional magnetic field modulated the plasmonic effects on Au nanoparticle's photocatalytic reactions triggered by separately applied visible lights.

Conclusions

The material characterization presented that only a few Au atoms fixed and formed tiny nanoparticles on the surface of the TiO_2 nanoparticles. The tiny Au nanoparticles lead to mutually enhanced photocatalytic reactions under an external magnetic field and plasmonic effects. The dominant enhancement by adding green light to the photocatalytic reaction leads to the understanding that it is a plasmonic effect. The positive results of adding EA in the experiments further present that it is a hot

electron dominant path photocatalytic reaction that is positively enhanced by both the external magnetic field and plasmonic effects.

Author contributions

HJ, YH, and XU conceived and carried out the experiments. HJ is the principal investigator of this research project. HJ, CYF, HP, and JCS designed the study, analyzed the data, and wrote the manuscript.

Conflicts of interest

There are no conflicts to declare.

Acknowledgements

This study was funded by the National Science and Technology Council, R.O.C., under contract numbers NSTC 111-2112-M-150-001, NSTC 112-2112-M-019-005, and NSTC112-2923-E-002-016. The authors thank the help of magnetic hysteresis measurements by Professor Huang-Wei Chang's lab in The Physical Department of National Chung Cheng University in Taiwan.

References

1 H. Raether, *Surface Plasmons on Smooth and Rough Surfaces and on Gratings*, Springer, Berlin/Heidelberg, Germany, 1988.
2 E. Hecht, *Optics*, Pearson Education, London, England, 2017.
3 K. Awazu, M. Fujimaki, C. Rockstuhl, J. Tominaga, H. Murakami, Y. Ohki, *et al.*, *J. Am. Chem. Soc.*, 2008, **130**, 1676–1680.
4 D. M. Schaadt, B. Feng and E. T. Yu, *Appl. Phys. Lett.*, 2005, **86**, 063106.
5 D. Derkacs, S. H. Lim, P. Matheu, W. Mar and E. T. Yu, *Appl. Phys. Lett.*, 2006, **89**, 093103.
6 N. Wu, *Nanoscale*, 2018, **10**, 2679–2696.
7 S. Singh, V. C. Srivastava and S. L. Lo, *Mater. Sci. Forum*, 2016, **855**, 105–126.
8 J. C. S. Wu, T. H. Wu, T. Chu, H. Huang and D. Tsai, *Top. Catal.*, 2008, **47**, 131–136.
9 H. J. Huang and B. H. Liu, *Catal. Commun.*, 2014, **43**, 136–140.
10 H. J. Huang, S. Y. Zhen, P. Y. Li, S. D. Tzeng and H. P. Chiang, *Opt. Express*, 2016, **24**, 15603–15608.
11 S. K. Cushing, J. Li, F. Meng, T. R. Senty, S. Suri, M. Zhi, *et al.*, *J. Am. Chem. Soc.*, 2012, **134**, 15033–15041.
12 J. Li, S. K. Cushing, F. Meng, T. R. Senty, A. D. Bristow and N. Wu, *Nat. Photonics*, 2015, **9**, 601–607.
13 C. Sönnichsen, T. Franzl, T. Wilk, G. von Plessen, J. Feldmann, O. Wilson, *et al.*, *Phys. Rev. Lett.*, 2002, **88**, 077402.
14 A. Sousa-Castillo, M. Comesaña-Hermo, B. Rodríguez-González, M. Pérez-Lorenzo, Z. Wang, X. T. Kong, *et al.*, *J. Phys. Chem. C*, 2016, **120**, 11690–11699.
15 X. Li, D. Xiao and Z. Zhang, *New J. Phys.*, 2013, **15**, 023011.
16 H. J. Huang, J. C. S. Wu, H. P. Chiang, Y. F. Chou Chau, Y. S. Lin, Y. H. Wang, *et al.*, *Catalysts*, 2020, **10**, 46.
17 M. Goddati, H. Q. Nguyen, S. Kang, B. B. Gicha, L. T. Tufa, N. Nwaji, *et al.*, *Small*, 2023, **19**, 2302980.
18 S. Mukherjee, F. Libisch, N. Large, O. Neumann, L. V. Brown, J. Cheng, *et al.*, *Nano Lett.*, 2013, **13**, 240–247.
19 H. J. Huang, B. H. Liu, J. Su, P. J. Chen, C. T. Lin, H. P. Chiang, *et al.*, *J. Phys. D: Appl. Phys.*, 2017, **50**, 375601.
20 R. Sundararaman, P. Narang, A. S. Jermyn, I. I. I. W. A. Goddard and H. A. Atwater, *Nat. Commun.*, 2014, **5**, 5788.
21 H. J. Huang, Y. H. Wang, Y. F. C. Chau, H. P. Chiang and J. C. S. Wu, *Nanoscale Res. Lett.*, 2019, **14**, 323.
22 Y. H. Wang, V. H. Dang, H. J. Huang and J. C. S. Wu, *Catal. Commun.*, 2023, **179**, 106691.
23 M. Wakasa, S. Suda, H. Hayashi, N. Ishii and M. Okano, *J. Phys. Chem. B*, 2004, **108**, 11882–11885.
24 M. Wakasa, N. Ishii and M. Okano, *C. R. Chim.*, 2006, **9**, 836–840.
25 H. Okumura, S. Endo, S. Joonwichien, E. Yamasue and K. N. Ishihara, *Catal. Today*, 2015, **258**, 634–647.
26 J. Li, Q. Pei, R. Wang, Y. Zhou, Z. Zhang, Q. Cao, *et al.*, *ACS Nano*, 2018, **12**, 3351–3359.
27 J. Kiwi, *J. Phys. Chem.*, 1983, **87**, 2274–2276.
28 W. Zhang, X. Wang and X. Fu, *Chem. Commun.*, 2003, 2196–2197.
29 M. Yamamoto, Y. Minoura, M. Akatsuka, S. Ogawa, S. Yagi, A. Yamamoto, *et al.*, *Phys. Chem. Chem. Phys.*, 2020, **22**, 8730–8738.
30 H. Lu, B. Zhao, R. Pan, J. Yao, J. Qiu, L. Luo, *et al.*, *RSC Adv.*, 2013, **4**, 1128–1132.
31 W. Gao, R. Peng, Y. Yang, X. Zhao, C. Cui, X. Su, *et al.*, *ACS Energy Lett.*, 2021, **6**, 2129–2137.
32 M. Ai, L. Pan, C. Shi, Z. F. Huang, X. Zhang, W. Mi, *et al.*, *Nat. Commun.*, 2023, **14**, 4562.
33 W. Gao, X. Zhao, T. Zhang, X. Yu, Y. Ma, E. C. dos Santos, *et al.*, *Nano Energy*, 2023, **110**, 108381.
34 T. Lv, J. Li, N. Arif, L. Qi, J. Lu, Z. Ye, *et al.*, *Matter*, 2022, **5**, 2685–2721.
35 L. Pan, M. Ai, C. Huang, L. Yin, X. Liu, R. Zhang, *et al.*, *Nat. Commun.*, 2020, **11**, 418.
36 X. B. Yuan, L. L. Cai, Y. L. Tian, G. C. Hu and J. F. Ren, *Appl. Surf. Sci.*, 2018, **427**, 156–161.
37 X. Li, W. Wang, F. Dong, Z. Zhang, L. Han, X. Luo, *et al.*, *ACS Catal.*, 2021, **11**, 4739–4769.
38 W. Gao, J. Lu, S. Zhang, X. Zhang, Z. Wang, W. Qin, *et al.*, *Adv. Sci.*, 2019, **6**, 1901244.
39 L. Lei, N. Wang, X. M. Zhang, Q. Tai, D. P. Tsai and H. L. W. Chan, *Biomicrofluidics*, 2010, **4**, 043004.
40 S. J. Jang, Y. C. Kang, J. S. Hyun, T. H. Shin, Y. W. Lee and K. C. Roh, *Catalysts*, 2021, **11**, 1196.
41 J. F. Moulder, *Handbook of X-Ray Photoelectron Spectroscopy: A Reference Book of Standard Spectra for Identification and Interpretation of XPS Data*, Physical Electronics Division, Perkin-Elmer Corporation, 1992.
42 J. Coutts, P. Hintze, A. Meier, R. Devor, J. Surma, P. Maloney, *et al.*, Visible-Light-Responsive Photocatalysis: Ag-Doped

TiO_2 Catalyst Development and Reactor Design Testing, in *46th International Conference on Environmental Systems*, 2016.

43 H. J. Huang, Y. C. Chiang, C. H. Hsu, J. J. Chen, M. H. Shiao, C. C. Yeh, *et al.*, *Sensors*, 2020, **20**, 1293.

44 T. P. Rossi, P. Erhart and M. Kuisma, *ACS Nano*, 2020, **14**, 9963–9971.

45 K. Wenderich and G. Mul, *Chem. Rev.*, 2016, **116**, 14587–14619.